Effects of Nb on the Microstructure and Properties of Ti-Added Hypereutectic High-Cr Cast Iron

J.P. Lai, Q.L. Pan, X.D. Wang, H.R. Cui, and Y.W. Sun

Effects of Nb on the microstructure and properties of Ti-added hypereutectic high-Cr cast iron were studied. With the addition of Nb, a new phase (Nb,Ti)C was formed. The microstructure analysis revealed that the amount of primary carbides was decreased from 18.6 to 8.8% and the primary and eutectic carbides were greatly refined. The decrease in the amount of primary carbides was attributed with the shrinking of primary M_7C_3 phase zone in the phase diagram, while the refinement of primary carbides was attributed to the heterogeneous nucleus of (Nb,Ti)C phase for the primary M_7C_3 carbides. The macrohardness of the alloy increased from 60.8 to 63.5HRC, and the impact toughness increased from 3.8 to 5.2 J cm^{-2}. Furthermore, the wear resistance was enhanced with the addition of Nb due to the formation of hard (Nb,Ti)C carbides.

1. Introduction

Hypereutectic high-Cr cast iron has a wide range of applications in slurry pumps and mining industries where serious work condition is required due to its large volume fraction of primary M_7C_3 carbide (Ref 1). However, the coarse primary M_7C_3 carbides in the hypereutectic high-Cr cast iron can wreck the continuity of the matrix and accelerate the forming and expanding of the crack (Ref 2). Therefore, the refinement of the coarse primary M_7C_3 carbides is beneficial to increase the fracture toughness and enlarge the application of hypereutectic high-Cr cast irons.

Alloying with titanium and niobium has been proved to be an effective way to refine the microstructure and improve the wear resistance (Ref 3-6). The refinement mechanism has been proved to be the heterogeneous nucleation TiC/NbC particles serving as for the primary M_7C_3 carbides (Ref 3-6). This refinement mechanism is often discussed based on two points: (a) the formation of TiC carbides prior to primary M_7C_3 carbides and (b) the possibility of TiC carbides acting as heterogeneous nucleating substrate of M_7C_3 carbides using the disregistry theory (Ref 7, 8). Chung et al. (Ref 9) found that the microstructural change from a hypereutectic alloy to a hypoeutectic one was due to the consumption of carbon depleted by Ti to form TiC carbides. Filipovic et al. (Ref 10) found the addition of 0.26%Ti can change the morphology and distribution of NbC carbides in high-Cr cast iron, which is deduced as the heterogeneous nucleation of TiC for NbC. A few data were discussed on the formation and structure of (Nb,Ti)C carbides.

In this paper, niobium and titanium were jointly added into the hypereutectic high-Cr cast iron to investigate the effects of niobium on microstructure and properties of Ti-added hypereutectic high-Cr cast iron.

2. Experimental Procedures

Table 1 lists the chemical composition of the high-chromium cast irons. The alloys investigated were melted in a medium-frequency induction furnace and cast at into a cylindrical metal mold with dimensions of $\Phi200 \times 300$ mm. Specimens for microstructural observation and abrasive wear tests were cut from the cast bars using wire-electrode cutting machines. Figure 1 shows the schematic drawing of retrieving samples from the cast bars for microstructural analysis and abrasive wear test. The surface A represents the microstructural observation surface.

All specimens were destabilized at 950 °C for 3 h, followed by quenching in the air at room temperature and then tempered at 200 °C for 3 h to release stress. Specimens for microstructural observation were mechanically polished and then etched by a 3% nital solution. Microstructure was investigated by scanning electron microscope (SEM, Sirion 200) and electron probe micro-analyzer (EPMA, JMA-8230). The microhardness tests were carried out on a microhardness tester (BUEHLER 5104) by a 20 g load for 15 s. Each of the data of microhardness was obtained by averaging at least five measurements. X-ray diffraction (XRD, Rigaku D/max 2500) was performed with a scanning speed of 2°/min. The differential scanning calorimetry (DSC, TAS100) was carried out with a heating rate of 10 °C/min. Impact toughness tests were determined on unnotched specimens (10 mm × 10 mm × 55 mm) with an impact-testing machine (JB-300B). Each of the data was achieved by averaging three measurements.

The three-body abrasive wear test was performed on the MLS-225 rubber wheel abrasive tester with a contact load of 100 N. The slurry consisted of 1000 mL of distilled water and 1500 g of sand (50-70 mesh silica sand). The specimens with dimensions of $55 \times 25 \times 6$ mm were mechanically polished

J.P. Lai, Q.L. Pan, X.D. Wang, H.R. Cui, and **Y.W. Sun**, School of Materials Science and Engineering, Central South University, Changsha 410083, People's Republic of China. Contact e-mail: 270746431@qq.com.

Table 1 Chemical composition of the high-chromium white cast iron (wt.%)

Alloy	C	Si	Mn	Cr	Mo	Ti	Nb
A	3.08	1.21	0.80	20.1	1.02	1.05	0.00
B	3.10	1.19	0.81	20.2	1.01	1.01	2.05
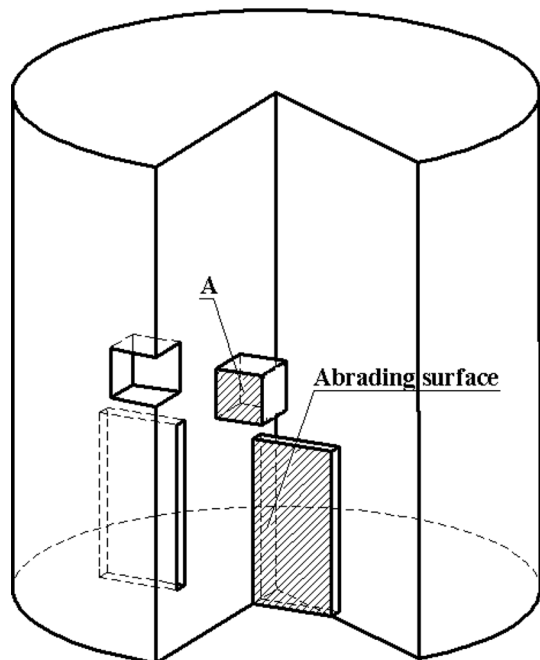
Fig. 1 A schematic drawing of retrieving samples from the cast bars

before abrasive wear test. The test was carried out at a rotating speed of 240 rpm for 25 min. The weight loss was measured on an analytical balance with a resolution of 0.001 g.

3. Results and Discussion

3.1 As-Cast Microstructure

Figure 2 shows the as-cast microstructures of the alloys. With the addition of Nb, the needle-like primary M_7C_3 carbides are refined to a rod or polygon shape. The average length of primary M_7C_3 carbides is decreased from 180 μm for the alloy A to 75 μm for the alloy B. Meanwhile, the amount of primary M_7C_3 carbides is decreased from 18.6% for the alloy A to 8.8% for the alloy B by using Leica digital images analyzer.

EPMA examination was used to analyze the microstructure more clearly, as shown in Fig. 3. The primary and eutectic carbides are refined with the addition of Nb. The matrix of alloy A is composed predominantly of pearlite and some retained austenite, while the matrix of alloy B consists of retained austenite. The bright particles in the alloy B are distributed accompanying the primary M_7C_3 carbides. Further magnification of the red squares in Fig. 2(a) and (b) reveals that the darker particles (point B) and the bight particles (point D) exist in the primary M_7C_3 carbides. The EPMA analysis, as listed in Table 2, indicates that the darker particles (point B) and the brighter particles (point D) may be of TiC type and composite

(Nb,Ti)C carbides, respectively. The volume fraction of (Nb,Ti)C carbides is measured to be 4-6% by using Leica digital images analyzer, while the TiC is difficult to be measured due to its small size and weak contrast difference with other phases. According to the ratios of Nb/Ti and M(Nb and Ti)/C, the bright particle is identified to be $(Nb_{0.8}Ti_{0.2})C_{0.96}$. The pearlitic matrix (Point A) in the alloy A possesses the higher carbon content than the retained austenite (Point C) in the alloy B.

Figure 4 presents the XRD and DSC results of the as-cast alloys. It is found that the emergence of NbC peaks indicates the formation of NbC carbides with the addition of Nb. It should be noted that the diffraction peak angles of NbC were 34.86° and 40.52°, while the corresponding peak angles from PDF card were 34.73° and 40.32°. This may be due to lattice distortion resulting from the substitution of Nb with Ti atom in the NbC lattice. This can decrease lattice distance (d) because the atom radius of Ti is a little smaller than that of Nb. According to the Bragg equation: $2d\sin\theta = \lambda$, because λ is a constant, when lattice distance d decreased, diffraction angle θ increased. Therefore, the diffraction angles of NbC carbides increased compared with the corresponding peaks angles of PDF card. The eutectic reaction temperature of hypereutectic high-Cr cast iron was predicted in the range from 1217 to 1276 °C (Ref 11). The temperature of eutectic reaction of the alloy A is 1268 °C, which is identical with that of the alloy B.

Figure 5 shows the phase diagram of Fe-3.1C-20Cr-1.2Si-0.8Mn-1.0Mo-1.0Ti system with 0 and 2wt.% niobium addition by using the thermodynamic database of Thermo-Calc software (Fe7). From the phase diagram, the carbon content marked by the dashed lines is closer to the eutectic reaction point for the alloy B than for the alloy A, thus resulting in the shrinking of primary carbide zone from a-b section to A-B section. The shrinking of primary carbide zone is responsible for the decrease in the amount of primary carbides from 18.6 to 8.8% in the microstructure, which may be associated with the consumption of carbon depleted by Nb to form NbC carbides. The eutectic reaction temperature of the two alloys is 1299 °C, while the DSC analysis of the two alloys indicates that the eutectic reaction temperature of the two alloys is 1268 °C, which may be due to the non-equilibrium solidification condition for the alloys.

3.2 Formation of (Nb,Ti)C Phase

Figure 6 shows the mapping element distribution of the (Nb,Ti)C carbides analyzed by EMPA. As shown in Fig. 6, the carbides are enriched in Nb and Ti elements and essentially free from Cr element and the Cr is rejected from forming the (Nb,Ti)C carbides. The distribution of Nb is homogenous in the carbides, while the concentration of Ti exhibits a degressive trend from the core to outershell of (Nb,Ti)C phase. According to relevant the literature (Ref 12, 13), the standard Gibbs formation free energy (ΔG_{NbC}^L and ΔG_{TiC}^L) in iron melt are calculated using Eq 1 and 2, respectively.
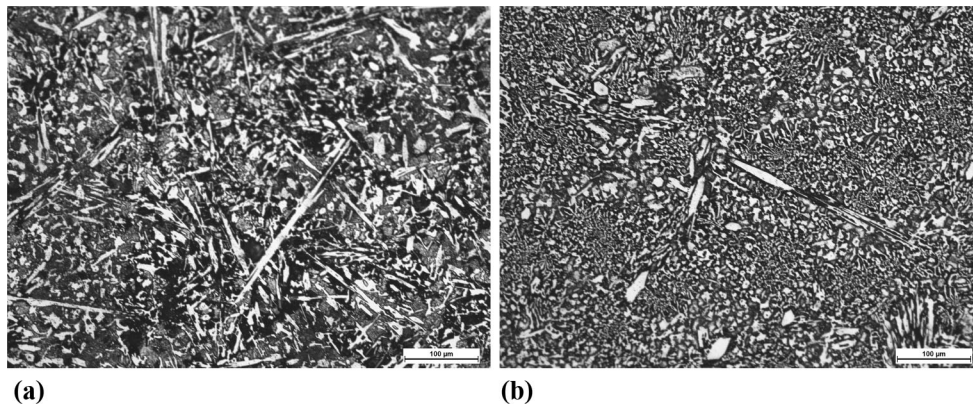
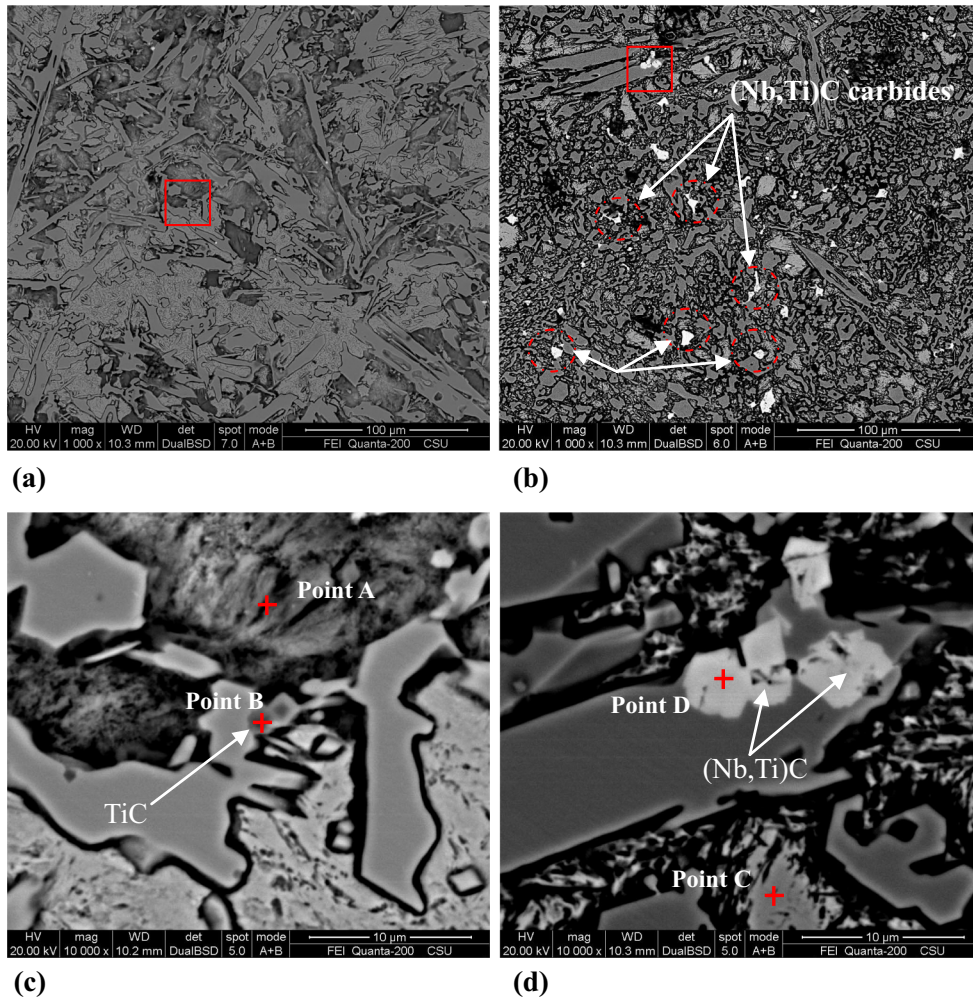**Fig. 2** As-cast metallurgical microstructure of the alloys: (a) alloy A; (b) alloy B

Fig. 3 SEM images of the as-cast alloys: (a, c) alloy A; (b, d) alloy B

Table 2 Chemical composition of different phases analyzed by EPMA (at.%)

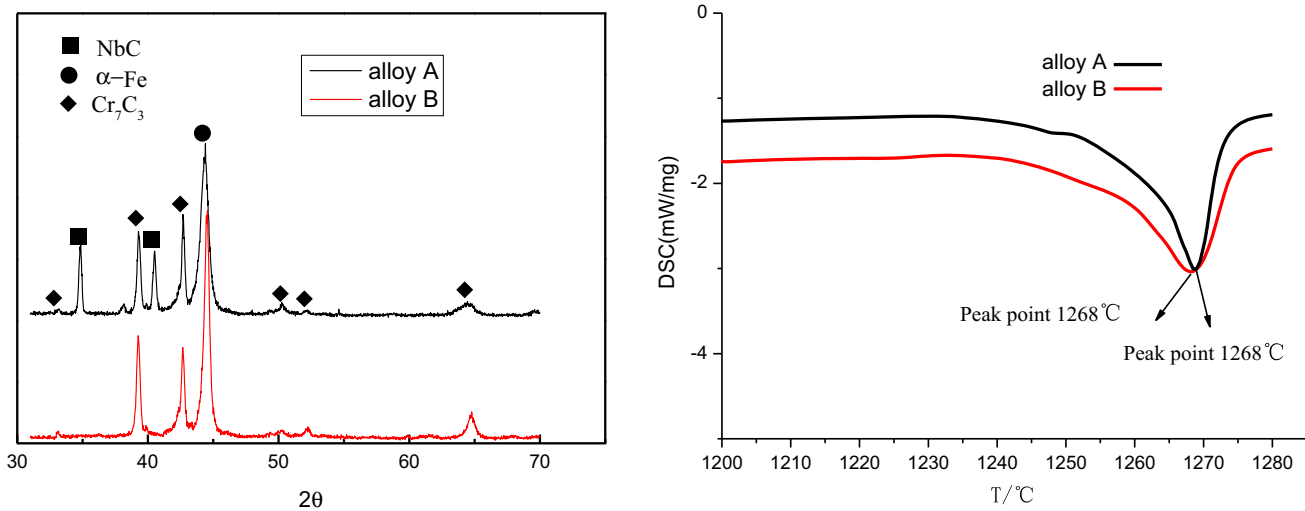| Positions	C	Si	Mn	Cr	Mo	Ti	Nb	Fe
A	1.6 ± 0.1	2.9 ± 0.1	0.4 ± 0.05	12.1 ± 0.5	0.3 ± 0.1	…	…	Bal.
B	48.1 ± 2.0	…	…	2.5 ± 0.2	0.3 ± 0.1	49.2 ± 2.0	…	Bal.
C	11.3 ± 1.0	2.2 ± 0.1	0.4 ± 0.05	11.8 ± 0.5	0.3 ± 0.1	…	…	Bal.
D	48.5 ± 2.0	…	…	0.3 ± 0.1	0.6 ± 0.1	10.1 ± 1.0	40.5 ± 0.1	Bal.

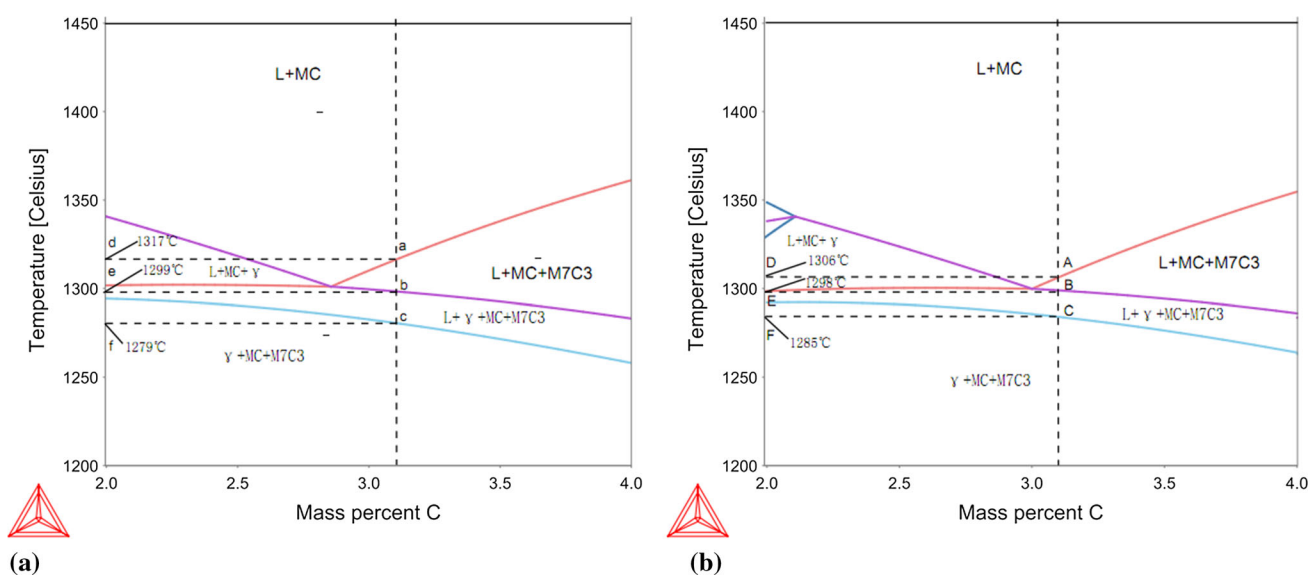**Fig. 4** The XRD patterns and DSC curves of the as-cast alloys

(a)

(b)

Fig. 5 The phase diagram: (a) Fe-3.1C-20Cr-1.2Si-0.8Mn-1.0Mo-1.0Ti alloy and (b) Fe-3.1C-20Cr-1.2Si-0.8Mn-1.0Mo-1.0Ti-2.0Nb alloy

$$[Ti] + [C] = TiC(s), \quad \Delta G_{NbC}^{L} = -189110 + 100.44T \text{ J/mol}$$
(Eq 1)

$$[Nb] + [C] = NbC(s), \quad \Delta G_{TiC}^{L} = -219000 + 38T \text{ J/mol}$$
(Eq 2)

The ΔG of NbC and TiC is calculated as $-151,626$ and -11029.88 J/mol, respectively, by substituting the melting temperature of high-Cr cast iron (1773 K) into Eq 1 and 2 (Ref 12). It is postulated that NbC formed firstly in the melt, because the ΔG of NbC is lower than that of TiC, suggesting that the NbC phase possesses a larger nucleation driving force than the TiC phase. However, the (Nb,Ti)C phase is identified in the microstructure rather than the NbC phase. The reason is discussed as follows: As solidification processes, the atom sites of Nb in the lattice are substituted by the Ti atoms. The substitution of Nb atom with Ti atom occurs easily in the NbC lattice, because the atom radius of Ti and Nb is similar

and both of TiC and NbC lattices are face-centered cubic structure (FCC). As a result, the (Nb,Ti)C phase came into being in the as-cast microstructure. The presence of composite (Nb,Ti)C phase in the high-Cr cast iron is also observed by Wang et al. (Ref 14).

3.3 Refinement Mechanism of M_7C_3 Carbides

The refinement mechanism of primary carbides with the addition of Nb or Ti has been verified that TiC/NbC particles act as the heterogeneous nuclei substrates for primary M_7C_3 carbide (Ref 12, 14, 15). Liu et al. (Ref 6) proved the heterogeneous nucleation theory of NbC for the primary M_7C_3 carbide by molecular dynamics simulation and first-principles calculations. The formation temperature of (Nb,Ti)C is higher than that of M_7C_3 carbides (Ref 10). Therefore, during the solidification process, (Nb,Ti)C phase formed firstly in the melt, which was found accompanying with the
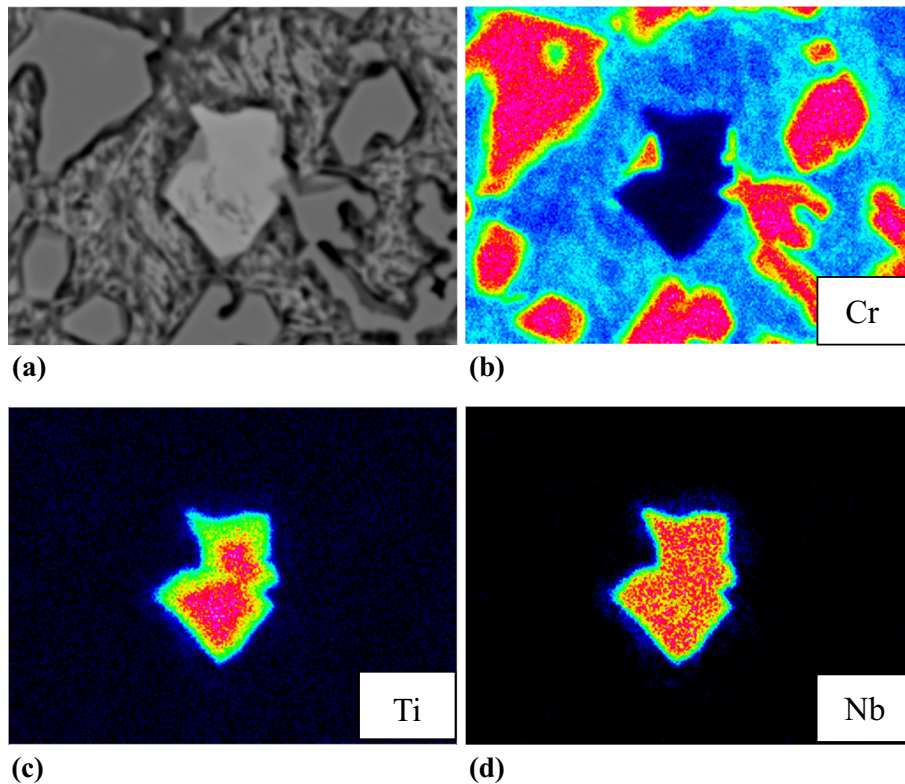
Fig. 6 Distribution of elements of the (Nb,Ti)C carbides by EPMA: (a) alloy B; (b, c, d) distribution of Cr, Ti and Nb, respectively

M_7C_3 carbides, so it is deduced that (Nb,Ti)C particles can serve as heterogeneous nucleus for the M_7C_3 carbides.

The lattice structure of (Nb,Ti)C phase is the face-centered cubic structure, and the M_7C_3 carbides have the close-packed hexagonal structure. The most probable plane of M_7C_3 nucleating on the (Nb,Ti)C is $(010)_{M7C3}$ nucleating on the $(110)_{(Nb,Ti)C}$ (Ref 14, 16). The (Nb,Ti)C composition is identified to be $(Nb_{0.8}Ti_{0.2})C_{0.96}$ by EPMA analysis. Referring to the relevant literature (Ref 14, 16, 17), the lattice parameters of $(Nb_{0.8}Ti_{0.2})C_{0.96}$ and M_7C_3 phases are obtained. Figure 7 shows the lattice correspondence of the crystal plane $(110)_{(Nb,Ti)C}$ and $(010)_{M7C3}$. The classical lattice disregistry (δ) model is used to estimate whether the (Nb,Ti)C phase can act as the heterogeneous nuclei for the M_7C_3 carbides using Eq 3 (Ref 7, 8).

$$\delta_{(hkl)_n}^{(hkl)_s} = \sum_{i=1}^{3} \frac{\left| d_{[uvw]_s}^i \cos(\theta) - d_{[uvw]_n}^i \right|}{d_{[uvw]_n}^i} \times 100\% \qquad (Eq\ 3)$$

where $(hkl)_s$ and $[hkl]_s$ are the low index plane and the low index direction of the nucleus, respectively; $(hkl)_n$ and $[uvw]_n$ are the low index plane and the low index direction of the new phase, respectively.

According to Bramfitt's theory (Ref 8), the nuclei with $\delta < 6\%$ are very effective, less effective when δ is between 6 and 12%, and useless when $\delta > 12\%$. Table 3 shows lattice parameters and the calculation results of the lattice misfit between the crystal plane $(010)_{M7C3}$ and $(110)_{(Nb,Ti)C}$. The lattice misfit (δ) is calculated to be 4.18%. Therefore, (Nb,Ti)C can serve as the heterogeneous nuclei for the primary M_7C_3 carbide and refine the primary carbides.
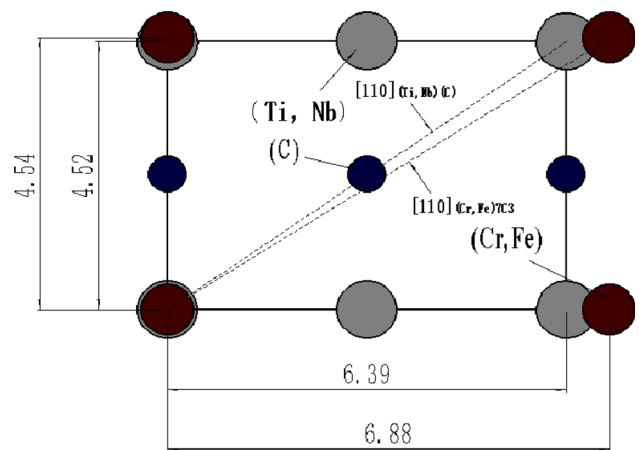

Fig. 7 Lattice correspondence of the crystal plane $(110)_{(Nb,Ti)C}$ and $(010)_{M7C3}$

3.4 Microstructure After Heat Treatment

Figure 8 presents the SEM micrographs of the alloys subjected to destabilization treatment. As shown in Fig. 8, the primary and eutectic carbides were not changed by destabilization treatment, while the pearlitic/austenitic matrix of the alloys transformed into martensitic matrix with precipitation of secondary carbides. Further magnification of the eutectic matrix (the red squares) revealed that the matrix of the alloy A precipitates denser and coarser secondary carbides. The secondary carbides precipitated from the matrix by absorbing the carbon and chromium elements. Higher carbon content of the as-cast pearlitic matrix in the alloy A contributed to the denser

secondary carbides precipitated, as listed in Table 2, because the higher carbon content in the matrix can provide more driving force for the precipitation of secondary carbides during destabilization treatment.

3.5 Mechanical and Wear Properties

As listed in Table 4, with the addition of Nb, the macro-hardness increases from 60.8 to 63.5HRC, the impact tough-ness increases from 3.8 to 5.2 J cm^{-2} and the weight loss decreases from 0.35 to 0.23 g. However, the microhardness of eutectic matrix in the alloy A is 920HV, higher than that in the alloy B (878HV), which is attributed to the denser secondary

carbides resulting in better particle dispersion strengthening effect. The macrohardness is influenced by the matrix, carbides type and CVF (carbide volume fraction). The CVF of M$_7$C$_3$ carbides depending on the composition of C and Cr is nearly same for the both alloys due to the same composition. Therefore, the difference of the alloys A and B is mainly affected by the matrix hardness and formation of (Nb,Ti)C carbides. The higher macrohardness in the alloy B arises from two competing effects: (a) The lower microhardness of eutectic matrix tends to decrease the macrohardness, and (b) the formation of (Nb,Ti)C carbides with hardness of 2700HV tends to increase the macrohardness. This indicates that the contri-bution of (Nb,Ti)C carbides accounts for a greater role on the

Table 3 Parameters and calculation results of the disregistry

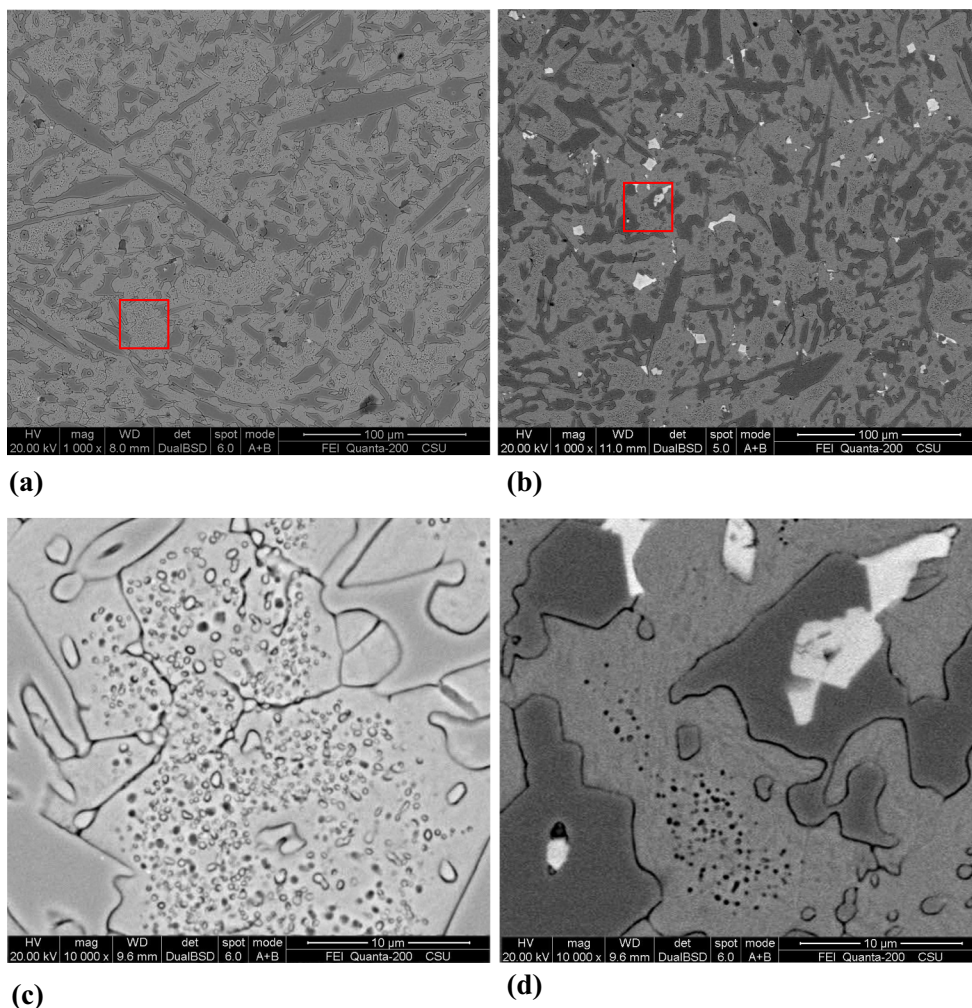| Results	$(110)_{(Nb0.8Ti0.2C)} \parallel (010)_{M7C3}$		
$[uvw]_{(Nb0.8Ti0.2C)}$	[100]	[010]	[110]
$[uvw]_{(M7C3)}$	[100]	[010]	[110]
θ, °	0	0	2.40
$d_{(Nb0.8Ti0.2C)}$, Å (Ref 13)	4.52	6.39	7.83
$d_{(M7C3)}$, Å (Ref 16)	4.54	6.88	8.24
δ, %		4.18	

Fig. 8 Microstructure after destabilizing heat treatment at 1000 °C for 2 h: (a, c) alloy A; (b, d) alloy B

Table 4   The mechanical properties of the alloys after heat treatment

Alloy	Microhardness of matrix, HV	Macrohardness, HRC	Impact toughness, J cm^{-2}	Weight loss, g
Alloy A	920 ± 10	60.8 ± 1	3.8 ± 0.4	0.35 ± 0.05
Alloy B	878 ± 10	63.5 ± 1	5.2 ± 0.4	0.23 ± 0.05
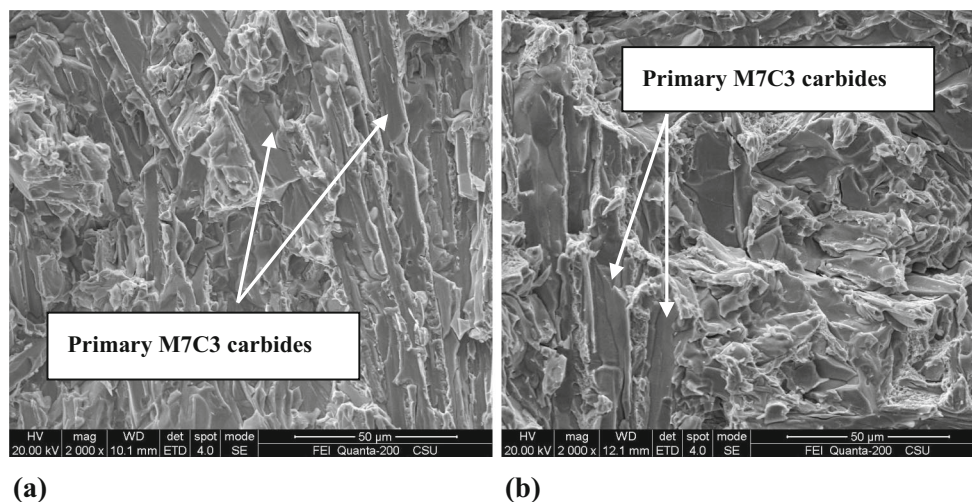
Fig. 9   Fracture morphologies of impact toughness specimens

effect of the macrohardness than the decrease in eutectic matrix microhardness.

Figure 9 shows the impact fracture morphologies of the alloys after destabilization treatment. Both alloys presented typically a character of brittle fracture. Shorter and less cleavage facets resulting from the fracture of primary carbides were observed in the alloy B, implying the better impact toughness. The straight cleavage facets were reported to be formed by localized delamination of cleavage cracks along primary carbides–matrix interfaces (Ref 18). The fracture crack is initiated preferentially at the brittle primary M_7C_3 carbides and tends to propagate through these carbides. Therefore, the decrease in the primary M_7C_3 carbide and their refinement with the addition of Nb is responsible for the improvement in impact toughness.

The secondary electrons (Fig. 10a and c) and backscattered electrons (Fig. 10b and d) of the SEM technique are used to characterize the worn surfaces of the samples. The mechanism of the three-body abrasion is composed of microcutting and plastic deformation (Ref 19). The wear mechanism is dominated by the microcutting in this case, which occurred predominantly in the coarse primary M_7C_3 carbides. Note that carbide cracking and fracture were evidently observed in both alloys, while the matrix was not damaged with little scratches along the sliding direction. The primary carbides in the alloy B showed less cracking level in the primary carbides due to the presence of (Nb,Ti)C carbides, which can provide protection effect to the primary carbides and matrix from suffering wear. According to the abrasive wear mechanism proposed by Kusumoto et al. (Ref 20), the carbides with higher hardness can provide good protection to the matrix, leaving little damage and a shadow zone without damage of the matrix behind them. In this case, the microhardness ranking of the phases can be organized as follows: NbC carbide > primary M_7C_3 carbide > eutectic M_7C_3 carbides > tempered martensite. During wear test, the NbC carbides were prior to suffer abrasives than other phases due to its highest hardness. When the NbC carbides were spalled by the abrasive particles and then detached from the worn surface, the primary carbides were getting ready to suffer the wear due to their hardness ranking. As shown in Fig. 11, it can be seen that the NbC carbides were spalled into small NbC particles by abrasive particles. However, the primary carbides in the alloy A were damaged more seriously due to the lack of hard carbides contributing to the higher weight loss. This was in agreement with weight loss measured and indicated a better wear resistance with the addition of Nb.

Figure 12 shows the different cracking level of primary and eutectic carbides. This is of importance to analyze the wear sequence of microstructural phases during wear test. As shown in Fig. 12, the cracking level of primary carbides is severer than that of the eutectic carbides. Similar result was obtained by Hanlon et al. (Ref 21). This is due to the higher hardness of primary carbides, which can protect the eutectic carbides from suffering wear, leaving little damage to eutectic carbides. This is of great evidence to illustrate the protection effect of hard carbides for the relatively soft phases in the microstructure. The presence of the amount of (Nb,Ti)C carbides with the highest hardness in the alloy B is the main role in contributing the less weight loss due to the protection effect of (Nb,Ti)C carbides.
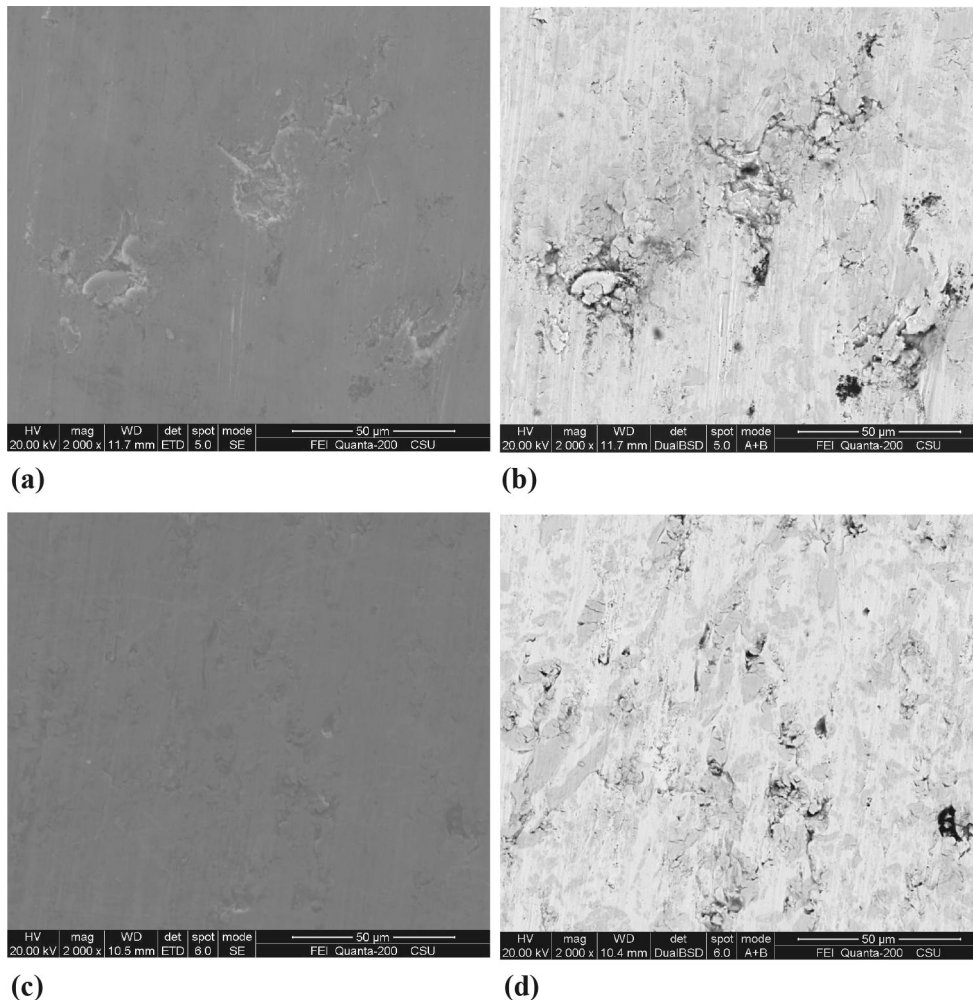
Fig. 10 SEM images of worn surfaces: (a, b) alloy A; (c, d) alloy B
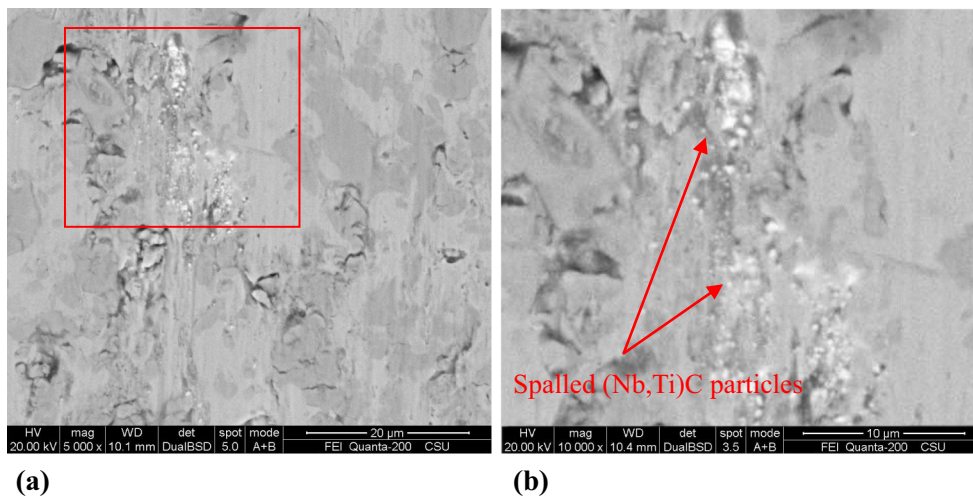

Spalled (Nb,Ti)C particles

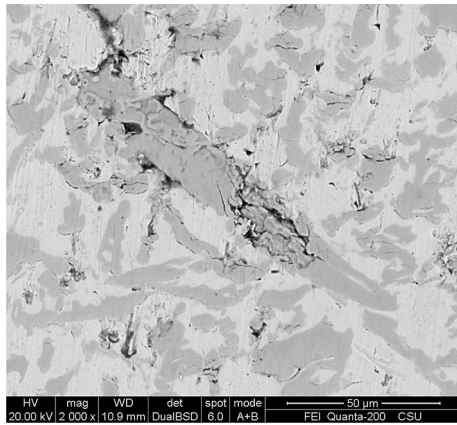**Fig. 11** The spalling of (Nb,Ti)C carbides during wear test

Fig. 12 SEM images of cracking of primary carbides

4. Conclusions

1. With the addition of Nb, finer primary M_7C_3 carbides and eutectic carbides are obtained and the amount of primary carbides is reduced. Moreover, a new phase (Nb,Ti)C is formed.
2. The decrease in the amount of primary M_7C_3 carbides is attributed to the shrinking of primary M_7C_3 phase zone in the phase diagram, while the refinement of primary M_7C_3 carbides is related to the heterogeneous nucleus of (Nb,Ti)C phase for the primary M_7C_3 carbides.
3. With the addition of Nb, the macrohardness of the alloy increased from 60.8 to 63.5HRC, while the impact toughness increased from 3.8 to 5.2 J cm^{-2}. And the wear resistance was also enhanced with the addition of Nb.

References

1. X.H. Zhi, J.Z. Liu, J.D. Xing, and S.Q. Ma, Effect of Cerium Modification on Microstructure and Properties of Hypereutectic High Chromium Cast Iron, *Mater. Sci. Eng. A*, 2014, **603**, p 98–103
2. X.H. Zhi, J.D. Xing, Y.M. Gao, H.G. Fu, J.Y. Peng, and B. Xiao, Effect of Heat Treatment on Microstructure and Mechanical Properties of a Ti-Bearing Hypereutectic High Chromium White Cast Iron, *Mater. Sci. Eng. A*, 2008, **487**, p 171–179
3. X.J. Xu, J.D. Xing, H.G. Fu, and X.H. Zhi, Effect of Titanium on the Morphology of Primary M_7C_3 Carbides in Hypereutectic High Chromium White Iron, *Mater. Sci. Eng. A*, 2007, **457**, p 180–185
4. X.H. Zhi, J.D. Xing, H.G. Fu, and Y.M. Gao, Effect of Titanium on the As-Cast Microstructure of Hypereutectic High Chromium Cast Iron, *Mater. Character.*, 2008, **59**, p 1221–1226
5. X.H. Zhi, J.D. Xing, H.G. Fu, and B. Xiao, Effect of Niobium on the As-Cast Microstructure of Hypereutectic High Chromium Cast Iron, *Mater. Lett.*, 2008, **62**, p 857–860
6. S. Liu, Z.J. Wang, Z.J. Shi, Y.F. Zhou, and Q.X. Yang, Experiments and Calculations on Refining Mechanism of NbC on Primary M_7C_3 Carbide in Hypereutectic Fe-Cr-C Alloy, *J. Alloys Compd.*, 2017, **713**, p 108–118
7. D. Turnbull and B. Vonnegut, Nucleation Catalysis, *Ind. Eng. Chem.*, 1952, **44**, p 1292–1298
8. B. Bramfitt, The Effect of Carbide and Nitride Additions on the Heterogeneous Nucleation Behavior of Liquid Iron, *Metall. Trans.*, 1970, **1**, p 1987–1995
9. R.J. Chung, X. Tang, D.Y. Li, B. Hinckley, and K. Dolman, Effects of Titanium Addition on Microstructure and Wear Resistance of Hypereutectic High Chromium Cast Iron Fe-25wt.%Cr-4wr.%C, *Wear*, 2009, **267**, p 356–361
10. M. Filipovic, Z. Kamberovic, M. Korac, and M. Gavrilovski, Microstructure and Mechanical Properties of Fe-Cr-C-Nb White Cast Irons, *Mater. Des.*, 2013, **47**, p 41–48
11. H.W. Zhang, Q. Liu, H. Shibata, Q. Wang, P. Jonsson, J.C. He, and K. Nakajima, Partial Equilibrium Prediction of Solidification and Carbide Precipitation in Ti-Added High Cr Cast Irons, *ISJI, Int.*, 2014, **54**, p 374–383
12. H.S. Ding, S.Q. Liu, H.L. Zhang, and J.J. Guo, Improving Impact Toughness of a High Chromium Cast Iron Regarding Joint Additive of Nitrogen and Titanium, *Mater. Des.*, 2016, **90**, p 958–968
13. H. Ohtani, M. Hasebe, and T. Nishizawa, Calculation of the Fe-C-Nb Ternary Phase Diagram, *Calphad*, 1989, **13**, p 183–204
14. J.B. Wang, T.T. Liu, Y.F. Zhou, X.L. Xing, S. Liu, Y.L. Yang, and Q.X. Yang, Effect of Nitrogen Alloying on the Microstructure and Abrasive Impact Wear Resistance of Fe-Cr-C-Ti-Nb Hardfacing Alloy, *Surf. Coat. Technol.*, 2017, **15**, p 1072–1080
15. S. Liu, Y.F. Zhou, X.L. Xing, J.B. Wang, and Q.X. Yang, Refining Effect of TiC on Primary M_7C_3 in Hypereutectic Fe-Cr-C Harden-Surface Welding Coating: Experimental Research and First-Principles Calculation, *J. Alloys Compd.*, 2017, **691**, p 239–249
16. H.G. Fu, X.J. Wu, X.Y. Li, J.D. Xing, Y.P. Lei, and X.H. Zhi, Effect of TiC Particle Additions on Structure and Properties of Hypereutectic High Chromium Cast Iron, *J. Mater. Eng. Perform.*, 2009, **18**, p 1109–1115
17. G.P. Shveikin, V.A. Tskhai, and B.V. Mitrofanov, Dependence of Microhardness on the Parameters of the Electronic Structure of Cubic Carbides and Nitrides of Group IV-VI, Transition Metals, *Inorg. Mater.*, 1987, **23**, p 837–841
18. X.S. Jia, Q.G. Hao, X.W. Zuo, N.L. Chen, and Y.H. Rong, High Hardness and Toughness of White Cast Iron: The Proposal of a Novel Process, *Mater. Sci. Eng. A*, 2014, **618**, p 96–103
19. J. Penagos, F. Ono, E. Albertin, and A. Sinatora, Structure Refinement Effect on Two and Three-Body Abrasion Resistance of High Chromium Cast Irons, *Wear*, 2015, **340**, p 19–24
20. K. Kusumoto, K. Shimizu, X. Yaer, Y. Zhang, Y. Ota, and J. Ito, Abrasive Wear Characteristics of Fe-2C-5Cr-5Mo-5W-5Nb Multicomponent White Cast Iron, *Wear*, 2017, **376–377**, p 22–29
21. D.N. Hanlon, W.M. Rainforth, and C.M. Sellars, The Rolling/Sliding Wear Response of Conventionally Processed and Spray Formed High Chromium Content Cast Iron at Ambient and Elevated Temperature, *Wear*, 1999, **225**, p 587–599